

Lasing from a Quantum-Dot-Like Buried Heterostructure in an InP Nanobeam Cavity

Valdemar Bille-Lauridsen,^{1,2, a)} Rasmus Jarbøl,¹ Meng Xiong,^{1,2} Aurimas Sakanas,¹ Elizaveta Semenova,^{1,2} Kresten Yvind,^{1,2} and Jesper Mørk^{1,2}

¹⁾ *Department of Electrical and Photonics Engineering, Technical University of Denmark, Building 343, 2800 Kongens Lyngby, Denmark*

²⁾ *NanoPhoton - Center for Nanophotonics, Technical University of Denmark, Building 343, 2800 Kongens Lyngby, Denmark*

(Dated: 18 March 2026)

We report lasing from a lithographically defined buried heterostructure with an estimated lateral footprint of $(107 \text{ nm})^2$, embedded in an InP photonic-crystal nanobeam cavity. This represents the smallest laterally confined buried heterostructure gain region from which lasing has been observed. Despite etching of the active region during cavity definition and the associated risk of surface-related nonradiative recombination, optically pumped devices exhibit a clear lasing threshold and a narrow linewidth. By systematically varying the BH size, we investigate how the lasing threshold depends on the active volume under optical pumping. The estimated intrinsic threshold under ideal carrier injection is 57 nW, comparable to values reported for single quantum-dot nanolasers, highlighting the potential of quantum-dot-scale buried heterostructures as deterministic, scalable gain media for nanophotonic lasers.

Ultracompact semiconductor lasers are a key enabling technology for densely integrated photonic circuits. In these lasers, low energy consumption, high optical confinement, and deterministic gain placement are key requirements¹⁻⁴. Photonic crystal nanocavities provide small mode volumes and high quality factors⁵, enabling strong light-matter interaction⁶. As cavities and active regions decrease in size, it becomes increasingly challenging to achieve a large controlled overlap between the optical cavity field and the gain region. Self-assembled quantum dots (QDs) offer excellent emission properties and have enabled record-low-threshold nanolasers⁷. Yet their stochastic nucleation leads to poor spatial alignment with cavity modes, lowering fabrication yield, and limiting scalability⁸. Deterministic alternatives based on micro pillars, nanorods or site-selected growth improve positioning, but these approaches have different challenges⁹⁻¹³. In particular, these approaches do not readily translate to planar cavities such as two-dimensional photonic crystals or nanobeams with small mode volumes, where efficient operation requires the active region to be precisely located at the cavity field maximum. This is especially true for bowtie cavities, where the central features can reach 10 nm¹⁴.

Buried heterostructures (BHs), which are laterally confined quantum wells formed by lithography and regrowth, provide a scalable solution offering strong lateral carrier confinement and precise spatial definition of the active region¹⁵⁻¹⁷. Recently, photonic crystal lasers have achieved exceptionally low threshold using such a BH structure^{4,18}. However, in previous demonstrations, the BH dimensions are several hundred nanometers, far from the quantum-dot regime.

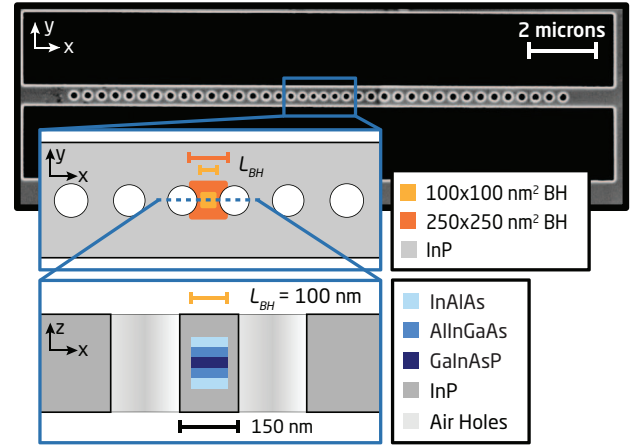


FIG. 1. Scanning electron microscope image of a fabricated nanobeam laser. A sketch of the central region is shown below, highlighting the scale of two different BH lengths l_{BH} as compared to the holes. At the bottom, the cross-section of the BH is illustrated.

In this work, we experimentally demonstrate lasing from buried heterostructures with estimated lateral dimensions between $\sim (107 \text{ nm})^2$ and $(216 \text{ nm})^2$ embedded in an InP photonic crystal nanobeam cavity. This represents the smallest laterally confined BH active region from which lasing has been reported. Despite the nearby etched surfaces, where nonradiative surface recombination is typically dominant in nanoscale III-V emitters^{19,20}, we observe a clear threshold transition and narrow linewidth under optical pumping. Lasing is enabled by careful surface passivation²¹ and strong spatial overlap between the cavity mode and the nanoscale BH. The smallest BH structures in this work are comparable to the size of early telecom-wavelength quantum dots, which also could have base diameters above 100 nm²².

^{a)} vchbi@dtu.dk

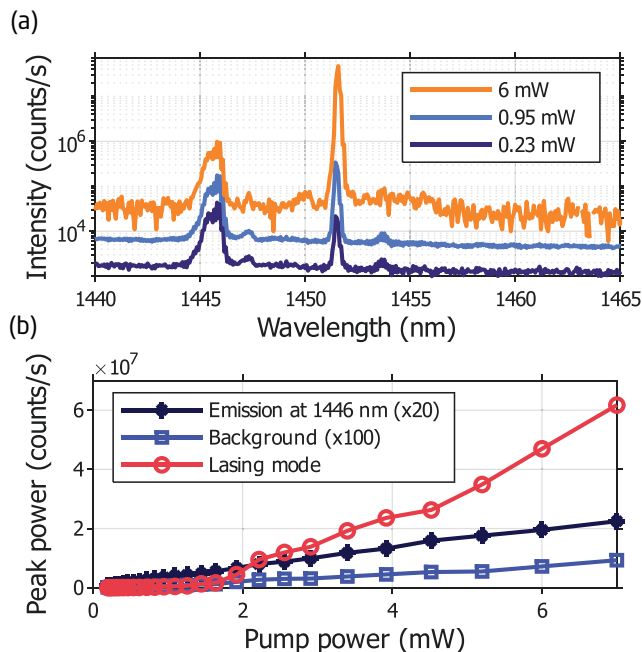


FIG. 2. (a) Emission spectra around the lasing wavelength measured far below, near, and above threshold. The spectrometer’s exposure time is greatly reduced above the threshold, leading to increased noise. (b) Pump power dependent peak emission intensity of the lasing mode compared to the emission around 1446 nm and the background, which is taken at 1460 nm.

The photonic crystal nanobeam cavities consist of a one-dimensional array of air holes with a linear tapered radius profile^{5,23}. The separation between the two central holes is designed to be 150 nm. This results in the BH being etched through during the cavity definition step for larger BH sizes [Fig. 1]. For smaller BHs, etch-through may still occur due to lithographic misalignment between the BH and cavity. Following cavity definition, the native oxide is removed using NH_4OH and $(\text{NH}_4)_2\text{S}$, where after a 7 nm layer of Al_2O_3 is deposited by atomic layer deposition for surface passivation²¹.

The cavity designs exhibit simulated quality factors exceeding $Q \simeq 10^5$ and effective mode volumes of $V_m \simeq 5(\lambda/2n)^3$. The fabricated devices have quality factors of $Q = 24.0(\pm 1.6) \times 10^3$, as determined by measuring nominally identical passive cavities following the approach of Galli et al.²⁴. Fabrication imperfections limit this value, most likely surface roughness, similar to previous reports on InP nanobeam cavities⁶.

The active region is based on an InP membrane incorporating a single GaInAsP quantum well and barrier layers [Fig. 1] grown by metal-organic vapour-phase epitaxy. The buried heterostructure is defined by electron-beam lithography and dry etching of a nanoscale mesa, followed by regrowth to laterally encapsulate the active material. The BH fabrication method is the same as described in a previous paper¹⁷. Scanning electron microscope (SEM) inspection of the HSQ mask reveals that the

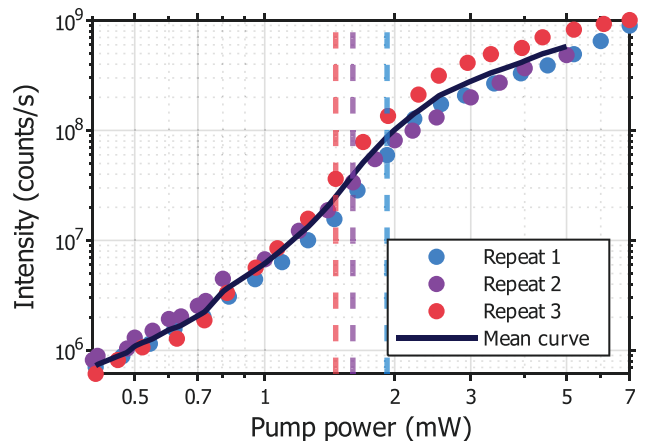


FIG. 3. Output versus external pump power for the smallest BH laser. Three repeated measurements, the average curve, and the extracted thresholds (vertical dashed lines) are shown.

realized mask sizes are systematically smaller than the nominal design values. Buried heterostructures with side lengths $l_{\text{BH,eff}} = 84(\pm 5)$ nm up to $l_{\text{BH,eff}} = 212(\pm 6)$ nm were fabricated, assuming that the active material size corresponds with the HSQ mask size.

We now present the performance of a device with an active region length of $l_{\text{BH,eff}} = 107(\pm 5)$ nm. This was the device with the smallest BH size for which lasing was confirmed. The devices are studied using two different experimental setups. In the first setup, the device is studied under continuous-wave optical pumping at $\lambda_p = 980$ nm through an objective with numerical aperture of 0.65, giving a diffraction-limited spot size of $A_{\text{spot}} \sim (750 \text{ nm})^2$. The output is collected using a spectrometer (SR-500i, Andor) with an InGaAs detector (iDus 1.7 μm , Andor), enabling reliable detection of low output powers. Figure 2 shows the emission spectra of the device. An additional peak is observed at 1446 nm together with a broadband background signal. Control measurements confirm that these features do not originate from the nanobeam device or the nanoscale BH, but from a much larger active region located nearby. When the pump spot is moved away from the nanobeam, the lasing mode disappears, whereas the 1446 nm peak and background emission remain²⁵. As the pump power increases, the mode at 1451 nm becomes dominant and exhibits a pronounced nonlinear increase in intensity, indicating the onset of lasing just below 2 mW, as shown in Fig. 2(b).

Measured input-output characteristics of the laser are shown in Fig. 3 on a log-log scale. The characteristic S-shaped curve associated with lasing is observed, from which the threshold is extracted as the pump power at which the derivative of the curve reaches its maximum²⁶. To account for variations in in-coupling efficiency due to pump spot alignment, the measurement was repeated three times. Although the pump spot is larger than the

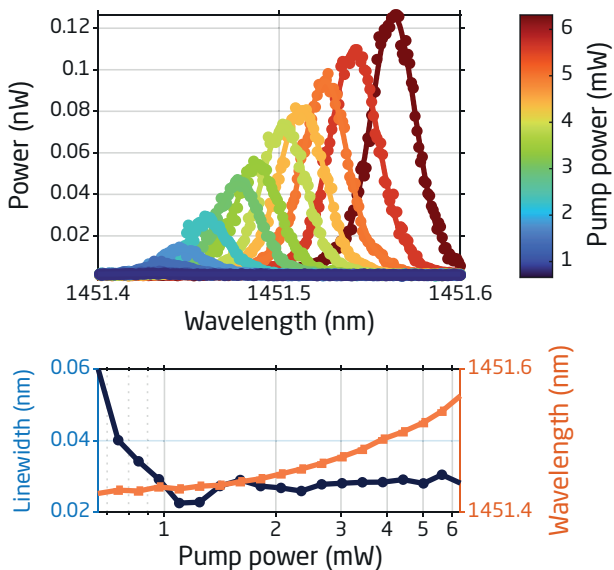


FIG. 4. The laser with $l_{\text{BH,eff}} = 107$ nm as measured in setup 2. (a): The fitted emission spectra at different pump powers. (b): From the fit of the spectra, peak wavelengths and widths are extracted and plotted as a function of the pump power. The pump powers in this figure cannot be directly compared to those in Figs. 2-3, as the injection efficiencies between the setups will differ.

BH sizes, the injection efficiency was found to be very sensitive to small changes in the pump spot position. The extracted thresholds from each trial are shown in the figure, indicating significant variation between measurements with a standard deviation of 0.24 mW.

To further confirm that the lasing threshold is reached, the devices were also characterized in a second setup. In the second setup, an optical spectrum analyzer (AQ6370D, Yokogawa) was used to measure the output, which provides improved spectral resolution. The results are shown in Fig. 4. Here, it is seen that the extracted linewidths are near the resolution limit of 0.02 nm, and are therefore likely limited by it. The linewidth observed at the lowest pump powers is quite uncertain due to the limited signal-to-noise ratio. The redshift at the highest pump powers is consistent with pump-induced heating and associated refractive-index changes^{27,28}.

In the next part of the paper, the comparative performance of lasers with larger BH sizes is considered. In addition to providing deterministic placement of a small active region, the BH technology also enables systematic control over its size. This allows us to study how the threshold of such a nanolaser depends on the size of the active medium. An input-output curve is captured for all fabricated devices with BH sizes ranging from 107 to 212 nm. For all these devices, a clear threshold was found. The extracted thresholds are shown as a function of the BH size in figure 5.

The intrinsic lasing threshold can be estimated from the steady-state gain-loss condition by assuming a log-

arithmic material gain, $g(N) = g_0 \ln(N/N_{\text{tr}})$, where g_0 is the gain coefficient and N_{tr} is the transparency carrier density²⁹. At threshold, the modal gain equals the cavity loss, $\Gamma v_g g(N_{\text{th}}) = 1/\tau_p$, where Γ is the optical confinement factor, v_g is the group velocity in the cavity, and τ_p is the photon lifetime. This yields the threshold carrier density

$$N_{\text{th}} = N_{\text{tr}} \exp\left(\frac{1}{\Gamma v_g g_0 \tau_p}\right). \quad (1)$$

From this expression, it is seen that a laser will operate close to the transparency $N_{\text{th}} \sim N_{\text{tr}}$, when the gain and confinement factor are high compared to the loss. The corresponding pump-power threshold can be estimated as

$$P_{\text{th}} = \frac{h\nu_p}{\eta_{\text{abs}}} \frac{V_{\text{act}}}{\tau_{\text{eff}}} N_{\text{th}}, \quad (2)$$

where $h\nu_p$ is the pump-photon energy, V_{act} is the active-region volume, η_{abs} is the injection efficiency, and τ_{eff} is the effective carrier lifetime defined by $\tau_{\text{eff}}^{-1} = \tau_r^{-1} + \tau_{nr}^{-1}$ with radiative and nonradiative lifetimes τ_r and τ_{nr} , respectively.

To better understand the measured results and the potential of the devices, we define an intrinsic threshold, which is the estimated threshold of the devices, under an ideal injection scheme. Under electrical injection, smaller active regions are expected to yield lower thresholds⁴. This follows directly from Eq. (2), as P_{th} scales approximately with $V_{\text{act}}/\eta_{\text{abs}}$. In the case of electrically pumped devices, η_{abs} can be close to unity, although leakage paths may play a role³⁰. Therefore, we define the intrinsic threshold P_{int} as the threshold power assuming perfect injection $\eta_{\text{abs}} = 1$.

However, in these experiments, the devices are optically pumped with a spot that is much larger than the active region. Consequently, only a small fraction of the incident power overlaps the BH. We account for this by expressing the absorbed pump fraction as

$$\eta_{\text{abs}} = \eta_0 \frac{A_{\text{act}}}{A_{\text{spot}}}, \quad (3)$$

where η_0 is the absorption efficiency for perfect spatial overlap, A_{spot} is the pump-spot area, and A_{act} is the lateral area of the active region. The active-layer thickness is $t = 8$ nm for all BH devices. In terms of power density, $p_{\text{th}} = P_{\text{th}}/A_{\text{spot}}$ the measured threshold becomes

$$p_{\text{th}} = \frac{h\nu_p t}{\eta_0 \tau_{\text{eff}}} N_{\text{tr}} \exp\left(\frac{1}{\Gamma v_g g_0 \tau_p}\right), \quad (4)$$

which is now not explicitly dependent on A_{act} . In this spot-limited regime, the local pump density, rather than the total carrier number, determines the threshold under optical pumping. Therefore, reducing the active area will not reduce the measured threshold.

TABLE I. Parameters used in the steady-state rate-equation model. The fitted absorbed pump fraction η_0 , is one order of magnitude below the theoretical upper limit of 17×10^{-3} as found by assuming that the absorption coefficient is $\alpha = 3 \times 10^4 \text{ cm}^{-1}$, similar to what is measured for InGaAs at a pump wavelength of 980 nm ³¹, and that the reflection from the top of InP surface is 27%.

| Symbol | Description | Value |
|---------------------|---|--------------------------------------|
| g_0 | Material gain parameter ³² | 3000 cm^{-1} |
| N_{tr} | Transparency carrier density ³² | $1.5 \times 10^{18} \text{ cm}^{-3}$ |
| τ_r | Radiative carrier lifetime ¹⁸ | 2 ns |
| τ_{nr} | Nonradiative carrier lifetime ²¹ | 5 ns |
| β | Spontaneous emission factor | 0.03 |
| η_0 | Absorbed pump fraction | 1.7×10^{-3} |
| η_{out} | Output coupling efficiency | 0.6×10^{-3} |

Theoretical thresholds were obtained by fitting steady-state semiconductor laser rate equations²⁹ to the experimental data. All model parameters were fixed except the spontaneous emission factor β , the absorption efficiency prefactor η_0 , and the output coupling efficiency η_{out} . Among these, only η_0 affects the theoretical threshold shown in Fig. 5. The remaining parameters are taken from literature values and are summarized in Table I. In the calculations, only the active volume V_{act} and the optical confinement factor Γ were varied between devices.

This model captures the overall trend observed in Fig. 5(a). The remaining deviation between experiment and theory is attributed to device-to-device variations that are not included in the model. In particular, the almost identical pair of devices with $l_{\text{BH}} \approx 145 \text{ nm}$, and $l_{\text{BH}} \approx 151 \text{ nm}$, exhibit noticeably different thresholds despite only a 6 nm difference in the BH size.

The scaling of the threshold with active region size depends on the carrier injection scheme. Under an ideal injection scheme, such as electrical injection, the relevant quantity is the total number of carriers required to reach transparency, $V_{\text{act}}N_{\text{tr}}$. Reducing the BH size therefore lowers the intrinsic threshold power P_{int} , as seen in Fig. 5(b). In this regime, the increase in threshold carrier density associated with a reduced optical confinement factor [Eq. (1)] leads to the flattening of the intrinsic threshold at the smallest BH sizes. In contrast, under optical pumping with a fixed pump spot, the threshold is governed by the local pump-induced carrier density rather than the total carrier number. As a result, the measured threshold increases for the smallest BHs due to the smaller confinement factor Γ under spot-limited optical pumping, as seen in Fig. 5(a), and explained by Eq. (4).

While this study employs optical pumping, the low internal threshold of quantum-dot-scale buried heterostructures can only be utilised with more ideal injection schemes. Importantly, electrical injection in similar nanobeam cavities has already been demonstrated^{3,33}. The estimated internal threshold of the lasers studied in this work is only slightly higher than the 42 nW

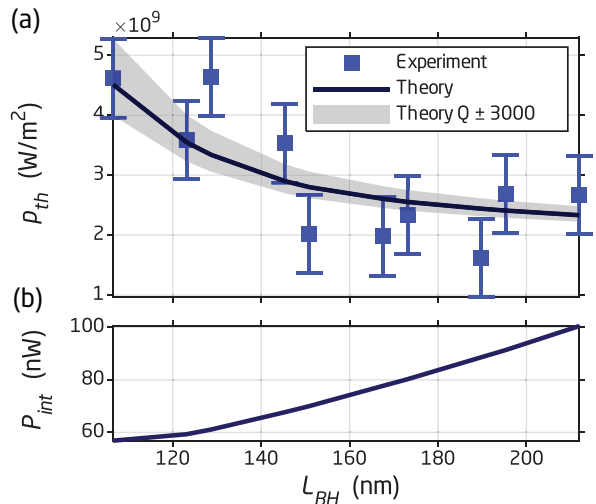


FIG. 5. The extracted thresholds are plotted as a function of the BH size, and with a steady-state rate-equation model. The error bars indicate the standard deviation as found in figure 3. In the lower part of the plot, the internal threshold is estimated assuming pumping with unity quantum efficiency ($\eta_{\text{abs}} = 1$).

threshold measured for a laser with a single stochastically grown quantum dot³⁴, representing nearly an order-of-magnitude reduction over lasers with larger BHs⁴ or multiple quantum dot layers³⁵.

For small BH structures, the logarithmic gain model overestimates the available gain, since it does not take full account of the bandfilling³⁶. This provides a plausible explanation for why lasing was not observed for the smallest fabricated BH device ($l_{\text{BH,eff}} = 84 \text{ nm}$), and indicates that improved Γ and/or higher Q will be required to reach threshold in this regime. One promising route is the use of dielectric bowtie nanocavities, which can provide substantially reduced mode volumes^{14,37}.

Interestingly, no significant increase in threshold is observed experimentally for larger BHs. This is the case even though these structures are etched through to a greater extent during cavity definition, exposing a larger fraction of the active region. While surface-related nonradiative recombination is often considered a fundamental limitation for deeply etched III-V nanostructures³⁸, the present devices all exhibit clear threshold behavior and narrow linewidth. This extends buried-heterostructure nanolasers into a previously unexplored lateral size regime and demonstrates that they can sustain efficient emission at lateral dimensions down to 100 nm.

With lateral dimensions approaching 100 nm, the results suggest that deterministic III-V gain media may be scaled into a quantum-dot-like size regime while retaining the material quality and reproducibility of epitaxial quantum well systems. Importantly, this reduction in active volume is achieved using a fabrication approach that is fully compatible with standard PhC cavity fabrication.

The ability to lithographically define the position and size of a quantum-dot-scale gain region opens opportunities for reproducible cavity–emitter coupling, dense integration, and systematic studies of light–matter interaction in the deep subwavelength regime³⁷.

ACKNOWLEDGMENTS

This work was supported by the Danish National Research Foundation through NanoPhoton - Center for Nanophotonics, Grant No. DNRF147

AUTHOR DECLARATIONS

Conflict of Interest

The authors have no conflicts to disclose.

Author Contributions

V. Bille-Lauridsen: Conceptualization (equal); Data Curation (lead); Formal Analysis (equal); Investigation (equal); Visualization (lead); Writing – original draft (lead); Writing – review and editing (equal); **R. Jarbøl:** Conceptualization (equal); Formal Analysis (equal); Investigation (equal); Writing – review and editing (equal); **M. Xiong:** Resources (equal); Supervision (equal); Writing – review and editing (equal); **A. Sakanas:** Conceptualization (equal); Resources (equal); Writing – review and editing (equal); **E. Semenova:** Project Administration (equal); Resources (equal); Supervision (equal); Writing – review and editing (equal); **K. Yvind:** Conceptualization (equal); Project Administration (equal); Supervision (equal); Writing – review and editing (equal); **J. Mørk:** Conceptualization (equal); Funding Acquisition (lead); Project Administration (equal); Supervision (equal); Writing – review and editing (equal);

REFERENCES

- J. L. O’Brien, A. Furusawa, and J. Vučković, “Photonic quantum technologies,” *Nature Photonics* **3**, 687–695 (2009).
- M. Notomi, “Manipulating light with strongly modulated photonic crystals,” *Reports on Progress in Physics* **73**, 096501 (2010).
- K.-Y. Jeong, Y.-S. No, Y. Hwang, K. S. Kim, M.-K. Seo, H.-G. Park, and Y.-H. Lee, “Electrically driven nanobeam laser,” *Nature Communications* **4**, 2822 (2013).
- E. Dimopoulos, M. Xiong, A. Sakanas, A. Marchevsky, G. Dong, Y. Yu, E. Semenova, J. Mørk, and K. Yvind, “Experimental demonstration of a nanolaser with a sub- μ A threshold current,” *Optica* **10**, 973 (2023).
- Y. Gong, B. Ellis, G. Shambat, T. Sarmiento, J. S. Harris, and J. Vučković, “Nanobeam photonic crystal cavity quantum dot laser,” *Optics Express* **18**, 8781 (2010).
- R. Ohta, Y. Ota, M. Nomura, N. Kumagai, S. Ishida, S. Iwamoto, and Y. Arakawa, “Strong coupling between a photonic crystal nanobeam cavity and a single quantum dot,” *Applied Physics Letters* **98**, 173104 (2011).
- Y. Ota, M. Kakuda, K. Watanabe, S. Iwamoto, and Y. Arakawa, “Thresholdless quantum dot nanolaser,” *Optics Express* **25**, 19981 (2017).
- L. Sapienza, M. Davanço, A. Badolato, and K. Srinivasan, “Nanoscale optical positioning of single quantum dots for bright and pure single-photon emission,” *Nature Communications* **6**, 7833 (2015).
- C. Schneider, T. Heindel, A. Huggenberger, P. Weinmann, C. Kistner, M. Kamp, S. Reitzenstein, S. Höfling, and A. Forchel, “Single photon emission from a site-controlled quantum dot-micropillar cavity system,” *Applied Physics Letters* **94**, 111111 (2009).
- P. J. Poole, D. Dalacu, J. Lefebvre, and R. L. Williams, “Selective epitaxy of semiconductor nanopillars for nanophotonics,” *Nanotechnology* **21**, 295302 (2010).
- S. Haffouz, K. D. Zeuner, D. Dalacu, P. J. Poole, J. Lapointe, D. Poitras, K. Mnamneh, X. Wu, M. Couillard, M. Korkusinski, E. Schöll, K. D. Jöns, V. Zwiller, and R. L. Williams, “Bright single inasp quantum dots at telecom wavelengths in position-controlled inp nanowires: The role of the photonic waveguide,” *Nano Letters* **18**, 3047–3052 (2018).
- P. Holewa, J. Jasiński, A. Shikin, E. Lebedkina, A. Maryński, M. Syperek, and E. Semenova, “Optical Properties of Site-Selectively Grown InAs/InP Quantum Dots with Predefined Positioning by Block Copolymer Lithography,” *Materials* **14**, 391 (2021).
- P. Holewa, A. Reiserer, T. Heindel, S. Sanguinetti, A. Huck, and E. Semenova, “Solid-state single-photon sources operating in the telecom wavelength range,” *Nanophotonics* **14**, 1729–1774 (2025).
- M. Xiong, Y. Yu, Y. Berdnikov, S. K. Borregaard, A. H. Dubré, E. Semenova, K. Yvind, and J. Mørk, “A nanolaser with extreme dielectric confinement,” *Science Advances* **11**, eadx3865 (2025).
- S. Matsuo, A. Shinya, T. Kakitsuka, K. Nozaki, T. Segawa, T. Sato, Y. Kawaguchi, and M. Notomi, “High-speed ultracompact buried heterostructure photonic-crystal laser with 13 fJ of energy consumed per bit transmitted,” *Nature Photonics* **4**, 648–654 (2010).
- A. Sakanas, *Buried Heterostructure Photonic Crystal Lasers*, Ph.D. thesis, Technical University of Denmark (2019).
- E. Dimopoulos, A. Sakanas, A. Marchevsky, M. Xiong, Y. Yu, E. Semenova, J. Mørk, and K. Yvind, “Electrically-Driven Photonic Crystal Lasers with Ultra-low Threshold,” *Laser & Photonics Reviews* **16**, 2200109 (2022).
- S. Matsuo, T. Sato, K. Takeda, A. Shinya, K. Nozaki, H. Taniyama, M. Notomi, K. Hasebe, and T. Kakitsuka, “Ultralow Operating Energy Electrically Driven Photonic Crystal Lasers,” *IEEE Journal of Selected Topics in Quantum Electronics* **19**, 4900311–4900311 (2013).
- C. F. Wang, A. Badolato, I. Wilson-Rae, P. M. Petroff, E. Hu, J. Urayama, and A. Imamoglu, “Optical properties of single InAs quantum dots in close proximity to surfaces,” *Applied Physics Letters* **85**, 3423–3425 (2004).
- S. Manna, H. Huang, S. F. C. Da Silva, C. Schimpf, M. B. Rota, B. Lehner, M. Reindl, R. Trotta, and A. Rastelli, “Surface passivation and oxide encapsulation to improve optical properties of a single gaas quantum dot close to the surface,” *Applied Surface Science* **532**, 147360 (2020).
- Y. Berdnikov, P. Holewa, A. Sakanas, J. M. Śmigiel, P. Mrowiński, E. Zikeba-Ostójk, K. Yvind, A. Huck, M. Syperek, and E. Semenova, “Efficient passivation of III-As(P) photonic interfaces,” (2025), arXiv:2502.08616 [physics].
- S. Anantathanasarn, R. Nötzel, P. J. Van Veldhoven, T. J. Eijkemans, and J. H. Wolter, “Wavelength-tunable (1.55- μ m region) InAs quantum dots in InGaAsP/InP (100) grown by metal-organic vapor-phase epitaxy,” *Journal of Applied Physics* **98**,

- 013503 (2005).
- ²³Q. Quan and M. Loncar, “Deterministic design of wavelength scale, ultra-high Q photonic crystal nanobeam cavities,” *Optics Express* **19**, 18529 (2011).
- ²⁴M. Galli, S. L. Portalupi, M. Belotti, L. C. Andreani, L. O’Faolain, and T. F. Krauss, “Light scattering and Fano resonances in high-Q photonic crystal nanocavities,” *Applied Physics Letters* **94**, 071101 (2009).
- ²⁵“Emission spectra from optically pump nanobeam lasers with nanoscale buried heterostructures,” <https://figshare.com/s/054705c587f0a2a709d5> (2025), the data supporting the presented findings.
- ²⁶M. Saldutti, Y. Yu, and J. Mørk, “The onset of lasing in semiconductor nanolasers,” *Laser & Photonics Reviews* **18**, 2300840 (2024).
- ²⁷M. Nomura, S. Iwamoto, K. Watanabe, N. Kumagai, Y. Nakata, S. Ishida, and Y. Arakawa, “Room temperature continuous-wave lasing in photonic crystal nanocavity,” *Optics Express* **14**, 6308 (2006).
- ²⁸Ling Lu, A. Mock, M. Bagheri, Jiang-Rong Cao, Sang-Jun Choi, J. O’Brien, and P. Dapkus, “Gain Compression and Thermal Analysis of a Sapphire-Bonded Photonic Crystal Microcavity Laser,” *IEEE Photonics Technology Letters* **21**, 1166–1168 (2009).
- ²⁹L. A. Coldren, S. W. Corzine, and M. L. Mašanović, *Diode Lasers and Photonic Integrated Circuits*, 2nd ed., Wiley Series in Microwave and Optical Engineering (John Wiley & Sons, Hoboken, NJ, 2012).
- ³⁰M. Marchal, E. Dimopoulos, K. Spiegelhauer, N. Chatzaras, M. Saldutti, K. Yvind, Y. Yu, and J. Mørk, “Carrier Transport in Electrically-Driven Photonic Crystal Membrane Lasers,” *Laser & Photonics Reviews*, e01579 (2025).
- ³¹B. Guo, B. Liang, J. Zheng, S. Ahmed, S. Krishna, A. Ghosh, and J. Campbell, “Digital alloy-grown inas/gaas short-period superlattices with tunable band gaps for short-wavelength infrared photodetection,” *ACS Photonics* **11**, 1419–1427 (2024), <https://doi.org/10.1021/acsp Photonics.3c01268>.
- ³²K. Seegert, *Theory and experimental characterization of nanostructured lasers*, Ph.D. thesis (2025).
- ³³G. Crosnier, D. Sanchez, S. Bouchoule, P. Monnier, G. Beaudoin, I. Sagnes, R. Raj, and F. Raineri, “Hybrid indium phosphide-on-silicon nanolaser diode,” *Nature Photonics* **11**, 297–300 (2017).
- ³⁴M. Nomura, N. Kumagai, S. Iwamoto, Y. Ota, and Y. Arakawa, “Photonic crystal nanocavity laser with a single quantum dot gain,” *Opt. Express* **17**, 15975–15982 (2009).
- ³⁵M. Nomura, S. Iwamoto, N. Kumagai, and Y. Arakawa, “Ultra-low threshold photonic crystal nanocavity laser,” *Physica E: Low-dimensional Systems and Nanostructures* **40**, 1800–1803 (2008).
- ³⁶J. Mørk, M. Xiong, K. Seegert, M. Marchal, G. Dong, E. Dimopoulos, E. Semenova, K. Yvind, and Y. Yu, “Nanostructured Semiconductor Lasers,” *IEEE Journal of Selected Topics in Quantum Electronics* **31**, 1–17 (2025).
- ³⁷V. Bille-Lauridsen, R. E. Christiansen, Y. Yu, and J. Mørk, “A deterministic approach for integrating an emitter in a nanocavity with subwavelength light confinement,” (2025), [arXiv:2512.19372](https://arxiv.org/abs/2512.19372) [physics.optics].
- ³⁸G. W. Bryant, “Quantum dots in quantum well structures,” *Journal of Luminescence* **70**, 108–119 (1996).